J. Fluid Mech. (2024), *vol*. 999, A31, doi:10.1017/jfm.2024.957

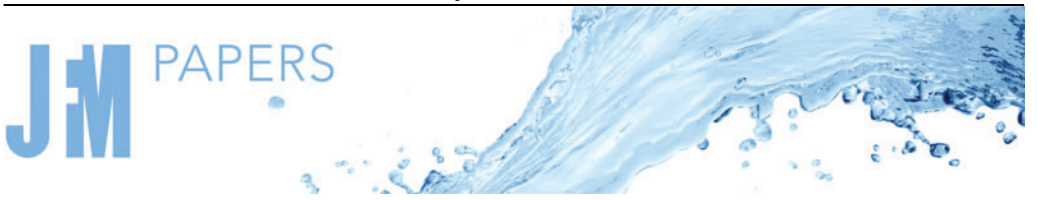

Interface evolution induced by two successive shocks under diverse reshock conditions

Qing Cao[1], Chenren Chen[1], He Wang[1,†], Zhigang Zhai[1] and Xisheng Luo[1,2,†]

[1]Advanced Propulsion Laboratory, Department of Modern Mechanics, University of Science and Technology of China, Hefei 230026, PR China

[2]State Key Laboratory of High-Temperature Gas Dynamics, Institute of Mechanics, Chinese Academy of Sciences, Beijing 100190, PR China

(Received 28 May 2024; revised 30 September 2024; accepted 30 September 2024)

The effects of reshock conditions, including the interface evolution state before reshock and the second shock intensity, on interface instability induced by two successive shocks propagating in the same direction are investigated via shock-tube experiments. It is observed that the reshock promotes the interface instability, and the post-reshock perturbation evolution relates to both the pre-reshock interface evolution state and second shock intensity. For the linear evolution of the twice-shocked interface, existing models perform poorly when either the pre-reshock interface shape effect or the secondary compression effect is pronounced, as current reduction factors fail to accurately describe these effects. Besides, the reshock-induced linear amplitude growth rate shows a non-monotonic dependence on the scaled pre-reshock amplitude, primarily due to the shape effect of the pre-reshock interface. For the post-reshock nonlinear evolution, the model proposed by Zhang & Guo (*J. Fluid Mech.*, vol. 786, 2016, pp. 47–61) offers reasonable predictions when the second shock is weak. However, when the second shock is moderately strong, the model overestimates the bubble growth and underestimates the spike evolution under the influence of the significant secondary compression effect. Furthermore, empirical linear and nonlinear models capable of describing the dependence of the post-reshock evolution on reshock conditions are proposed based on the present experimental results and existing models.

Key words: shock waves

1. Introduction

Richtmyer–Meshkov instability (RMI) occurs when a perturbed interface separating two fluids of different densities is impulsively accelerated by shock waves (Richtmyer 1960;

† Email addresses for correspondence: ustchewang@ustc.edu.cn, xsluo@imech.ac.cn

Meshkov 1969). It has attracted extensive attention for decades (Zhou 2017*a*,*b*; Zhou *et al.* 2019; Zhou *et al.* 2021; Zhou 2024) due to its crucial role in significant scientific and engineering fields such as inertial confinement fusion (ICF) (Nuckolls *et al.* 1972; Lindl *et al.* 2014), supernova explosion (Arnett *et al.* 1989; Kuranz *et al.* 2018) and scramjet (Billig 1993; Yang, Kubota & Zukoski 1993). Classical RMI induced by a single shock, referred to as single-shock RMI in this work, was first theoretically modelled by Richtmyer (1960) and later experimentally verified by Meshkov (1969). In subsequent decades of research, single-shock RMI was found to be sensitive to initial conditions such as initial amplitude (Rikanati *et al.* 2003; Wang *et al.* 2023*a*), interface morphology (Pandian, Stellingwerf & Abarzhi 2017; Liang *et al.* 2019), shock intensity (Holmes *et al.* 1999; Puranik *et al.* 2004) and Atwood number (Dimonte & Ramaprabhu 2010; Chen *et al.* 2023).

Notably, interface instability in practical applications is generally triggered by multiple shock waves. In ICF, the shock wave propagating towards the convergence centre would reflect back and re-impact the interfaces separating the ablator from deuterium–tritium ice and deuterium–tritium ice from deuterium–tritium gas. Therefore, RMI induced by two shock waves propagating in opposite directions, termed reflected-reshock RMI in the present study, has also garnered significant attention (Collins & Jacobs 2002; Balakumar *et al.* 2008, 2012; Lombardini *et al.* 2011; Balasubramanian *et al.* 2012). Specifically, substantial research has focused on investigating the influence of reshock conditions on post-reshock flow evolution. Reflected-reshock RMI at a single-mode interface was numerically investigated by Ukai, Balakrishnan & Menon (2011). The results showed that the post-reshock amplitude growth rate is weakly dependent on pre-reshock interface geometry but exhibits a linear relationship with the interface jump velocity induced by the reshock. Experimentally, Leinov *et al.* (2009) studied reflected-reshock RMI at an interface with randomly distributed small-scale perturbations. It was observed that the post-reshock evolution of the mixing zone is independent of its pre-reshock width but is strongly influenced by the reflected shock intensity. Subsequently, Balasubramanian *et al.* (2012) investigated reflected-reshock RMI at a single-mode gas curtain with various reshock timings using simultaneous planar laser-induced fluorescence (PLIF) and particle image velocimetry (PIV) techniques. The results clearly illustrated changes in mixing evolution and their dependence on the pre-reshock interface complexity. Later, Reilly *et al.* (2015) explored the influence of reshock timing on reflected-reshock RMI at a membraneless inclined planar interface, finding that a more developed pre-reshock interface leads to a more mixed post-reshock evolution. Using simultaneous PLIF and PIV techniques, Mohaghar *et al.* (2017, 2019) studied the effects of initial interface perturbation and shock intensity on the post-reshock mixing. The results indicated that the post-reshock flow maintains (loses) memory of the large-scale (small-scale) perturbation, and its evolution is related to the incident shock intensity. Recently, Guo *et al.* (2022*a*,*b*) conducted experiments on reflected-reshock RMI using well-defined initial interfaces created by the soap-film technique, revealing that the post-reshock evolution is sensitive to the pre-reshock interface profile. Additionally, it was observed that the high-amplitude effect of the pre-reshock interface promotes the mode interaction and enhances the nonlinear effects.

In addition to reflected-reshock RMI, interface instability induced by shock waves propagating in the same direction, referred to as 'S-RMI' in this study, is also prevalent in practical applications. For instance, in ICF, a drive scheme with shock waves propagating in the same direction is commonly employed to achieve the required drive pressure for ignition while maintaining the target shell at a relatively low entropy (Betti &

Hurricane 2016; Zhang *et al.* 2020; Abu-Shawareb *et al.* 2022). Given that interface perturbation can be significantly amplified in the prior evolution process, the additional shock impact may lead to virulent perturbation growth, thereby substantially reducing energy gain and potentially resulting in ignition failure (Dimonte & Ramaprabhu 2010). Therefore, investigating S-RMI is of great significance. However, currently, research on S-RMI remains scarce and insufficient compared with that on single-shock RMI and reflected-reshock RMI.

Theoretically, Mikaelian (1985) first proposed a linear superposition model to predict the linear amplitude growth rate of a twice-shocked interface ($\dot{a}_2^l$, where $\dot{a}$ represents the amplitude growth rate, with subscript '2' and superscript 'l' denoting parameters of twice-shocked interface and in the linear evolution period, respectively). Numerically, Charakhch'yan (2000, 2001) found that the linear superposition model is valid if reshock occurs at the linear evolution stage of the once-shocked interface. In contrast, if reshock occurs in the nonlinear evolution stage of the once-shocked interface, the linear superposition model is invalid, and the reshock-induced linear amplitude growth rate ($\Delta\dot{a}$) depends weakly on the scaled pre-reshock amplitude (ka_1^r, where k and a are wavenumber and amplitude, respectively, with subscript '1' and superscript 'r' denoting parameters of once-shocked interface and at the onset of reshock, respectively). Based on this observation, Charakhch'yan (2000, 2001) proposed an empirical model to forecast $\dot{a}_2^l$ in S-RMI with reshock occurring in the nonlinear evolution stage of the once-shocked interface. Subsequently, Karkhanis *et al.* (2017) numerically explored the ejecta phenomenon on the free surface of metal impulsively accelerated by two successive shocks, which can be treated as a limiting case of S-RMI. It was found that if reshock occurs in the nonlinear evolution stage of the once-shocked interface, the pre-reshock bubble deviates from a single-mode one and its profile effect can be described using the effective wavelength (Cherne *et al.* 2015). Additionally, a model proposed for the ejecta phenomenon induced by a single shock (Cherne *et al.* 2015) can also reasonably predict the reshock-induced ejecta production. Further, Karkhanis & Ramaprabhu (2019) found that the development of the post-reshock bubble can be accurately predicted by a potential flow model proposed for single-shock RMI (Mikaelian 1998). Additionally, an empirical model that accounts for both nonlinearity and compressibility (Karkhanis *et al.* 2018), also proposed for single-shock RMI, offers reasonable prediction for the terminal growth rate of the post-reshock spike. Williams & Grapes (2017) investigated the double-shock ejecta production in simulations considering material failure. It was found that if the spall failure occurs before reshock, the post-first-shock pressure field is subjected to perturbations with high amplitude and irregular structure. These perturbations were observed to have a significant influence on the post-reshock surface development. Recently, Wu *et al.* (2023) conducted a numerical investigation into the effect of the time interval between two shock impacts on the ejecta production from twice-shocked Sn. It was observed that if the time interval is short, the model proposed for ejecta induced by a single shock (Cherne *et al.* 2015) can well predict the reshock-induced ejecta mass when the profile effect of the pre-reshock interface is considered. However, when the time interval is long, the model significantly underestimates the reshock-induced ejecta mass even after considering the profile effect of the pre-reshock interface. This underestimation was ascribed to the promotion of reshock-induced ejecta generation by the first-shock-induced ejecta.

Experimentally, Dimonte *et al.* (1996) first observed the S-RMI phenomenon in the investigation of RMI induced by strong radiation-driven shocks. However, their focus was primarily on the effects of high Mach number and high initial amplitude on perturbation evolution, with less attention given to S-RMI. To study the ejecta on a twice-shocked metal, Buttler *et al.* (2014*a*,*b*) developed an explosively driven tool that can generate two

successive shocks. However, this experimental tool has limitations in studying S-RMI due to the complexity of the multi-physics coupling, challenges in generating controllable shocks and difficulties in diagnosing detailed experimental information (Wang *et al.* 2022). Relative to laser-driven or explosion-driven experiments, a shock-tube experiment offers a relatively simple physical environment and enables fine observation of flow evolution. Recently, Wang *et al.* (2022) designed a shock-tube facility capable of generating controllable successive shocks while ensuring that the interface would not be heavily affected by waves other than two primary shocks throughout the experiment. Using this facility, S-RMI on a single-mode light–heavy interface with reshock occurring in the linear evolution stage of the once-shocked interface was studied. It was found that $\dot{a}_2^l$ can be accurately predicted by the linear superposition model. Additionally, a nonlinear model proposed for single-shock RMI (Zhang & Guo 2016) provides a reasonable prediction for the weakly nonlinear evolution of the twice-shocked interface.

For ICF, the time interval between two successive shocks impacting an interface, as well as the intensity of the second shock, generally varies among different ignition schemes (Park *et al.* 2014; Betti & Hurricane 2016; Smalyuk *et al.* 2019). In other words, S-RMI occurring in ICF has diverse pre-reshock interface evolution states and second shock intensities (referred to as reshock conditions for clarity). Therefore, it is necessary and interesting to investigate the effects of reshock conditions on post-reshock interface evolution. Previous numerical studies (Charakhch'yan 2000, 2001; Karkhanis *et al.* 2017; Karkhanis & Ramaprabhu 2019; Wu *et al.* 2023) have provided some insights into the evolution laws of S-RMI with various pre-reshock interface evolution states, but relevant experimental research is still lacking. Furthermore, to our knowledge, there is currently no available investigation on the effect of the second shock intensity on post-reshock interface evolution. What is the dependence of the post-reshock interface evolution on reshock conditions? Can existing linear and nonlinear models correctly describe the evolution of the twice-shocked interface under diverse reshock conditions? These issues remain unclear, which motivates the present study. In this work, S-RMI with diverse reshock conditions is investigated via shock-tube experiments. The pre- and post-reshock flow features are first qualitatively discussed. Subsequently, the evolution law of the once-shocked interface and the characteristics of the pre-reshock interface are investigated. Following this, the dependence of the post-reshock linear amplitude evolution on reshock conditions is analysed, and models for predicting $\dot{a}_2^l$ are examined. Finally, the post-reshock nonlinear evolution law under different reshock conditions is investigated, and the applicability of an existing nonlinear model to forecast the evolution of the twice-shocked interface is explored.

2. Experimental methods

Experiments are performed in the specific shock-tube facility (Wang *et al.* 2022) illustrated in figure 1(*a*). The facility mainly includes two driver sections (A and B), a driven section, a transitional section, a stable section, a test section, two acrylic devices (I and II) and electronically controlled membrane rupture equipment. The principle of the facility in generating successive shocks, as well as varying the second shock intensity and the time interval between two shock impacts, has been illustrated in previous work (Wang *et al.* 2022), where readers can find further details. The soap-film technique, which has been extensively verified (Liu *et al.* 2018; Liang *et al.* 2019), is used to create the initial single-mode interface. As shown in figure 1(*b*), the transparent interface formation devices (1 and 2) are manufactured by combining two acrylic plates with pedestals. The formation

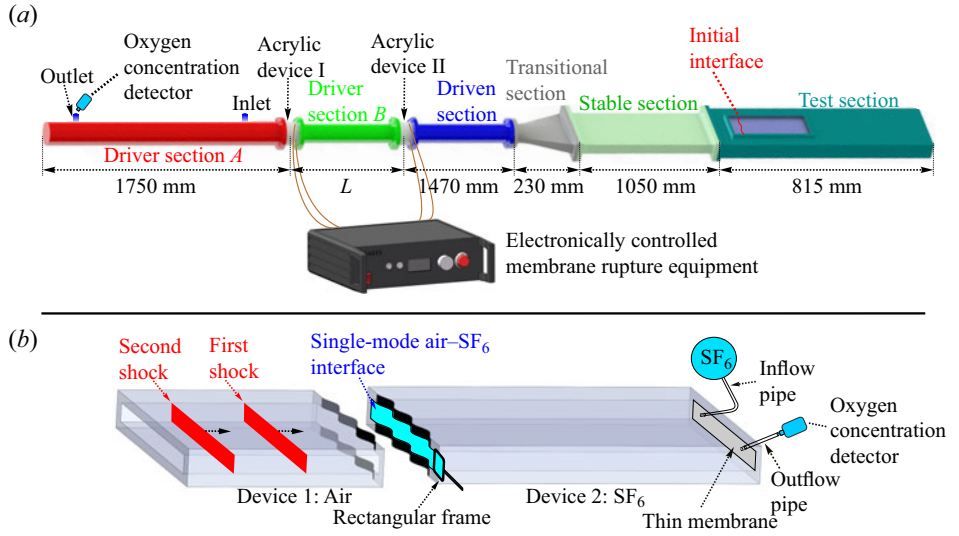

Figure 1. Sketches of the shock-tube facility for generating two successive shocks (*a*) and the interface formation devices (*b*).

process of the soap-film interface was detailed in previous work (Wang *et al.* 2023*a*) and is omitted here. The flow evolution is recorded by high-speed schlieren photography. The high-speed video camera (FASTCAM SA5, Photron Limited) operates at a frame rate of 50 000 frames per second, with an exposure time of 1 μs. The spatial resolution of the schlieren images is approximately 0.39 mm pixel^{-1}. In the following, the specific schemes for varying the reshock conditions in experiments are described in detail.

2.1. *Manipulation of pre-reshock interface evolution state*

For a once-shocked interface with a small initial amplitude, its evolution can be approximately divided into five successive stages: linear stage (interface evolves symmetrically), weakly nonlinear stage (interface evolves asymmetrically), moderately nonlinear stage (bubble and spike structures appear and become significant), strongly nonlinear stage (roll-up structures emerge) and turbulent mixing stage (multiscale vortices appear and materials are mixed intensely). Throughout the evolution process, the amplitude of the once-shocked interface continuously increases and its profile gradually deviates from a single-mode configuration (Collins & Jacobs 2002; Liu *et al.* 2018). The pre-reshock interface serves as the 'initial interface' for the second shock–interface interaction, and the combined effect of its high amplitude and non-single-mode profile on post-reshock evolution is collectively referred to as its shape effect.

In the present work, four evolution states of the pre-reshock interface (linear, weakly nonlinear, moderately nonlinear and strongly nonlinear) are considered to explore its shape effect on the post-reshock flow evolution. The evolution state of the pre-reshock interface depends primarily on factors including the initial amplitude (a_0), perturbation wavelength (λ), time interval between two shock impacts (Δt), first shock intensity and post-first-shock Atwood number ($A_1 = (\rho_1^d - \rho_1^u)/(\rho_1^d + \rho_1^u)$, where ρ is the density and superscripts 'u' and 'd' denote parameters of gases upstream and downstream of the interface, respectively). In this study, the evolution state of the pre-reshock interface is manipulated by altering a_0, λ and Δt to realize reshocks occurring at different evolution

stages of the once-shocked interface. The adjustment of a_0 and λ can be easily realized due to the flexibility of the soap-film technique in interface generation. Time interval Δt is varied by altering the distance between the generation positions of two shocks (L).

2.2. *Alteration of second shock intensity*

Previous studies on single-shock RMI (Sadot *et al.* 2003; Guo *et al.* 2020; Wang *et al.* 2023*b*) showed that the interface shape effect and the secondary compression effect introduced by transverse waves are coupled and jointly influence interface evolution. For S-RMI, it can be inferred that the pre-reshock interface shape effect and the secondary compression effect also couple and together affect the evolution of the twice-shocked interface. Consequently, to isolate the pre-reshock interface shape effect on post-reshock evolution, S-RMI with a very weak second shock is considered to minimize the secondary compression effect. In addition, S-RMI with weak and moderately strong second shocks are also considered to study how the twice-shocked interface evolves under the coupling of these effects.

The first shock is generated between the driven section and driver section B, containing air with pressures of 101.3 and 202.7 kPa, respectively. The polyester membrane separating the two sections has a thickness of 12.5 μm, and the Mach number of the first shock impacting the interface (M_1) is measured as 1.17 ± 0.01. According to previous work (Wang *et al.* 2022), the Mach number of the second shock impacting the interface (M_2) is positively correlated with that of the second shock initially generated between driver sections A and B (M_{2i}). The relation between M_{2i} and flow parameters (Glass & Hall 1959) is given by

$$\frac{p_a}{p_b} = \left[1 + \frac{2\gamma_b}{\gamma_b + 1}(M_{2i}^2 - 1)\right]\left[1 - \frac{\gamma_a - 1}{\gamma_b + 1}\frac{c_b}{c_a}\left(M_{2i} - \frac{1}{M_{2i}}\right)\right]^{-2\gamma_a/(\gamma_a - 1)}, \tag{2.1}$$

where subscripts 'a' and 'b' denote parameters of fluids in driver sections A and B, respectively; p, γ and c represent the pressure, specific heat ratio and sound speed of the gas, respectively. Therefore, M_2 can be modulated by changing the gas composition and pressure in driver section A. To generate a weak second shock, air is used as the gas in driver section A, with p_a of 405.3 kPa. The corresponding membrane separating driver sections A and B has a thickness of 30 μm, and M_2 is measured as 1.14 ± 0.01. For producing a very weak second shock, SF_6, which is considerably heavier than air, is utilized in driver section A, with p_a of 278.6 kPa. The thickness of the corresponding membrane is 10 μm, and M_2 is measured as 1.03 ± 0.01. To generate a moderately strong second shock, helium, which is significantly lighter than air, is employed in driver section A, with p_a of 683.9 kPa. The corresponding membrane has a thickness of 60 μm, and M_2 is measured as 1.40 ± 0.02.

In summary, three series of experiments with different second shock intensities (very weak, weak and moderately strong) are performed, each of which considers four pre-reshock interface evolution states (linear, weakly nonlinear, moderately nonlinear and strongly nonlinear). For clarity, the series of experiments with very weak, weak and moderately strong second shocks are labelled as cases VW, W and MS, respectively. Further, cases VW, W and MS with $ka^r_{1,e} = f$ (subscript 'e' denotes parameters extracted from experiments) are referred to as cases VW-f, W-f and MS-f, respectively. Some important parameters for the 12 experimental cases with diverse reshock conditions are summarized in table 1. The gas component downstream of the initial interface, A_1, and the post-reshock Atwood number ($A_2 = (\rho_2^d - \rho_2^u)/(\rho_2^d + \rho_2^u)$) are determined by assuming

Case	L	Δt	λ	ka_0	$v^i_{1,e}$	$v^i_{2,e}$	$u_{1,e}$	$u_{1,o}$	$u_{2,e}$	$u_{2,o}$	ϕ	A_1	A_2	M_1	M_2
VW-0.35	450	504	30	0.08	406.81	445.42	64.34	64.14	76.73	76.05	0.99	0.69	0.70	1.18	1.03
VW-0.70	450	584	30	0.17	401.79	433.70	58.80	57.38	65.88	64.84	0.99	0.69	0.69	1.16	1.02
VW-1.13	450	452	20	0.27	401.09	439.23	58.11	57.93	72.46	71.49	0.98	0.67	0.68	1.16	1.03
VW-1.78	550	822	20	0.27	402.04	439.12	56.60	57.98	70.50	70.65	0.99	0.69	0.70	1.16	1.03
W-0.32	700	459	30	0.08	401.79	480.11	59.88	60.14	112.81	113.18	0.99	0.68	0.70	1.17	1.14
W-0.71	700	547	30	0.17	406.43	488.07	64.84	64.51	119.68	118.93	0.99	0.69	0.71	1.18	1.15
W-1.19	700	444	20	0.27	405.36	484.67	63.82	64.57	117.45	116.86	0.99	0.69	0.71	1.18	1.14
W-1.88	900	947	20	0.27	397.60	472.23	56.15	55.43	108.87	106.51	0.99	0.69	0.71	1.16	1.14
MS-0.33	1250	513	30	0.08	402.05	574.36	57.25	58.06	191.03	192.80	0.99	0.69	0.74	1.16	1.40
MS-0.58	1250	472	30	0.17	400.15	563.80	55.27	56.25	184.31	184.65	0.99	0.69	0.74	1.16	1.38
MS-1.12	1250	461	20	0.27	400.30	572.92	55.80	56.29	189.97	191.85	0.99	0.69	0.74	1.16	1.40
MS-1.89	1450	984	20	0.27	401.79	572.92	58.22	57.63	193.53	192.95	0.99	0.68	0.73	1.16	1.40

Table 1. Some important parameters for experiments with diverse reshock conditions: L, distance between the generation positions of two shocks; Δt, time interval between two shock impacts; λ and ka_0, perturbation wavelength and scaled initial amplitude, respectively; $v^i_{1,e}$ and $v^i_{2,e}$, experimental velocities of the first and second incident shock waves, respectively; $u_{1,e}$ and $u_{1,o}$ ($u_{2,e}$ and $u_{2,o}$), velocities of once-shocked (twice-shocked) interface obtained from experiments and predicted by one-dimensional gas dynamics theory, respectively; ϕ, mass fraction of SF_6 at the downstream side of the initial interface; A_1 and A_2, post-first-shock and post-reshock Atwood numbers, respectively; M_1 (M_2), Mach number of the first (second) shock impacting the interface. Units of length, time and velocity are mm, μs and m s^{-1}, respectively, and similarly hereinafter.

that the upstream gas is pure air and matching the experimental and theoretical velocities of the once-shocked interface ($u_{1,e}$ and $u_{1,o}$, with subscript 'o' denoting parameters predicted by one-dimensional gas dynamics theory). The results of the shock and interface velocities, along with the Atwood numbers, suggest favourable experimental repeatability.

3. Results and discussion

3.1. *Flow features and interface morphology*

Schlieren images obtained from the experiments of cases VW, W and MS are shown in figures 2, 3 and 4, respectively. The temporal origin ($t = 0\,\mu$s) is defined as the moment when the first incident shock (IS_1) reaches the mean position of the initial interface. Note that the initial interface appears thick due to the sinusoidal filaments embedded on the interface formation device for constraining the soap film. Furthermore, the second incident shock (IS_2) in cases VW is not prominent in the experimental images due to its low intensity, and thus it is delineated by a blue dashed line for emphasis. It is evident that in cases with $ka^r_{1,e} < 0.4$, the pre-reshock interface shows an almost symmetric profile, suggesting that it remains within the linear evolution stage. For cases with $0.4 < ka^r_{1,e} < 1.0$, the pre-reshock interface no longer evolves symmetrically, signifying that it has entered the weakly nonlinear evolution stage. In cases with $1.0 < ka^r_{1,e} < 1.5$, the emergence of the bubble and spike structures indicates that the pre-reshock interface has progressed into the moderately nonlinear evolution stage. In contrast, for cases with $ka^r_{1,e} > 1.5$, the appearance of the roll-up structures indicates that the pre-reshock interface has advanced into the strongly nonlinear evolution stage.

Case W-0.32 is taken as an example to illustrate the evolution process of S-RMI with reshock occurring at the linear or weakly nonlinear evolution stage of the once-shocked interface. As illustrated in figure 3(a), when IS_1 encounters the initial interface, the first

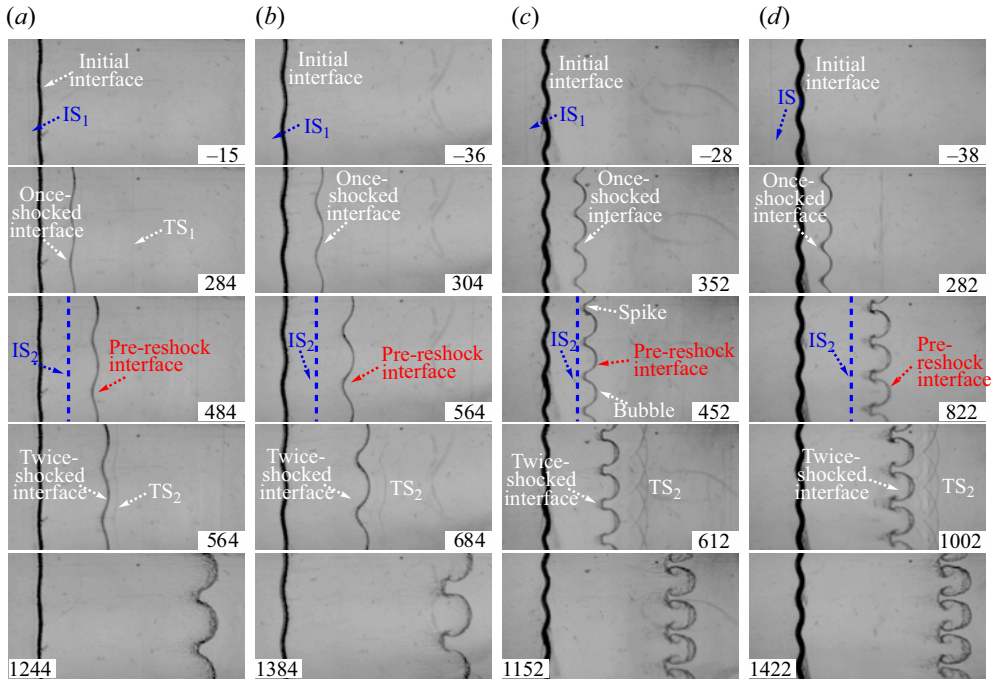

Figure 2. Experimental schlieren images of cases VW: (*a*) VW-0.35, (*b*) VW-0.70, (*c*) VW-1.13 and (*d*) VW-1.78. Here IS_1 and IS_2 (TS_1 and TS_2) are the first and second incident (transmitted) shock waves, respectively. Numbers represent time in μs.

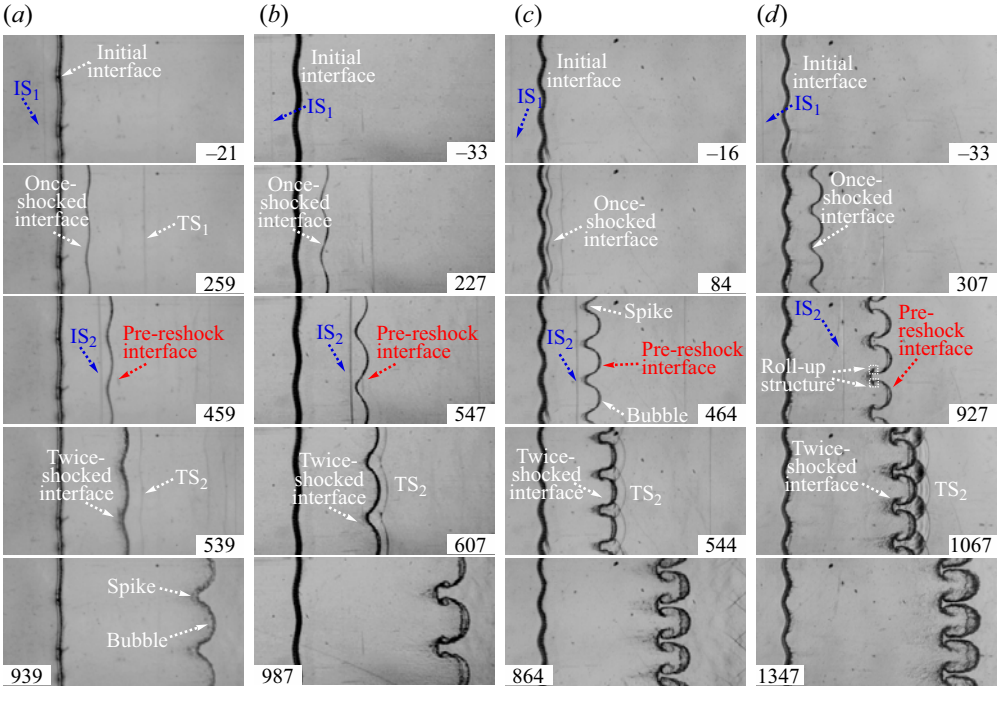

Figure 3. Experimental schlieren images of cases W: (*a*) W-0.32, (*b*) W-0.71, (*c*) W-1.19 and (*d*) W-1.88.

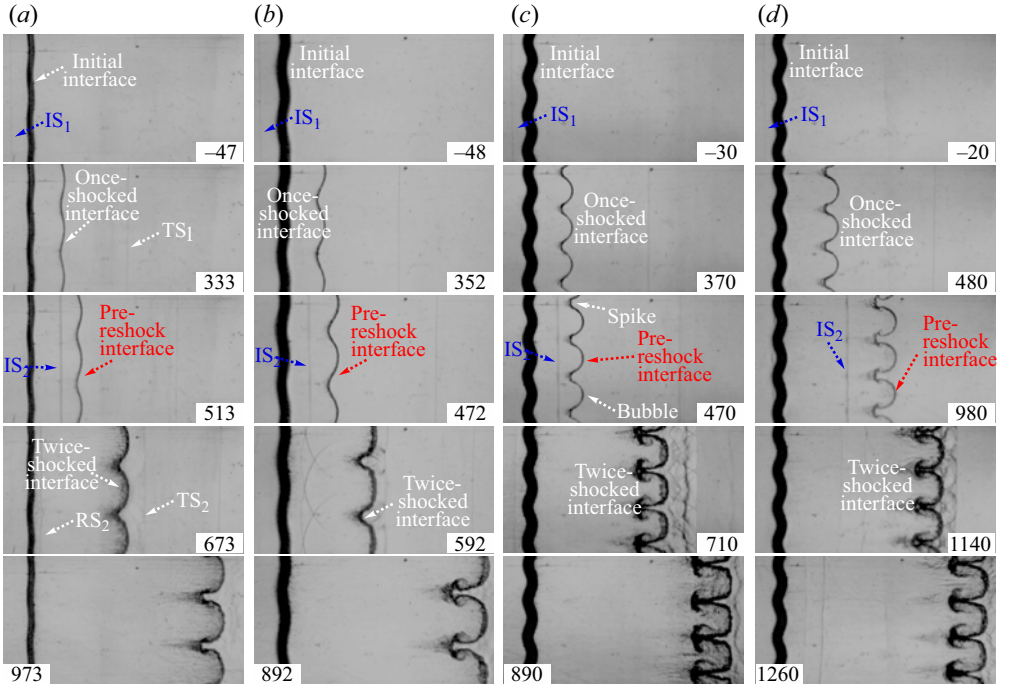

Figure 4. Experimental schlieren images of cases MS: (*a*) MS-0.33, (*b*) MS-0.58, (*c*) MS-1.12 and (*d*) MS-1.89. Here RS_2 is the second reflected shock.

transmitted shock (TS_1) and the first reflected shock (RS_1) are generated, in which RS_1 is difficult to identify clearly due to its weak intensity. Meanwhile, the once-shocked interface starts to evolve gradually under the drive of the baroclinic vorticity deposited by IS_1 and the pressure perturbations introduced by disturbed TS_1 and RS_1. When reshock occurs, the second transmitted shock (TS_2) and the second reflected shock (RS_2) are generated (539 μs), with RS_2 being too weak to be observed. Subsequently, the amplitude and asymmetry of the twice-shocked interface increase gradually, followed by the formation of distinct bubbles and spikes (939 μs). Notably, the twice-shocked interface evolves significantly faster than the once-shocked interface, indicating that the reshock promotes the interface instability. Then, case W-1.88 is taken as an example to illustrate the evolution process of S-RMI with reshock occurring at the moderately or strongly nonlinear evolution stage of the once-shocked interface. Due to the high amplitude of the pre-reshock interface, TS_2 is highly disturbed and its wavefront rapidly evolves into a series of Mach reflection configurations (1067 μs). The reflected shocks in the Mach reflection configurations, also referred to as transverse waves, continuously interact with the twice-shocked interface until TS_2 moves away from the latter, introducing the secondary compression effect (Motl *et al.* 2009; McFarland, Greenough & Ranjan 2013; Guo *et al.* 2020). For S-RMI on a light–heavy interface considered in the present work, the secondary compression effect would inhibit (promote) the growth of bubbles (spikes) as they evolve towards the downstream (upstream) direction. With the further evolution of the twice-shocked interface, the roll-up structures on both sides of the spikes become more pronounced (1347 μs). Simultaneously, the spike stems narrow while the bubbles expand in the spanwise direction.

Comparing the evolution of S-RMI with similar pre-reshock interface evolution states but various second shock intensities, several distinct features emerge when the second

shock is stronger. First, the twice-shocked interface evolves more rapidly. Second, the transverse waves are stronger, and the separation of TS_2 from the twice-shocked interface is slower. Third, the bubbles are flatter while the spikes are more slender. Specifically, in cases MS-1.12 and MS-1.89, the heads of the bubbles gradually flatten out and occupy nearly the entire space along the spanwise direction in the late stages. Similar bubble and spike evolutions were observed in previous studies on single-shock RMI with significant secondary compression effect (Motl *et al.* 2009; Stanic *et al.* 2012; Guo *et al.* 2020). Overall, the qualitative results show that the evolution of the twice-shocked interface is related to both the pre-reshock interface evolution state and the second shock intensity.

3.2. *Amplitude evolution*

Temporal variations of the scaled perturbation amplitude (ka) measured from experiments for cases VW, W and MS are shown in figures 5(a), 5(b) and 5(c), respectively. It is observed that the reshock promotes the perturbation amplitude growth, with a more pronounced effect when $ka^r_{1,e}$ is larger and/or the second shock is stronger. In all cases, the amplitude growth of the twice-shocked interface first undergoes a quasi-linear stage and then enters the nonlinear stage. The following discussion and analysis will address the three fundamental issues of S-RMI: the evolution law of the once-shocked interface, the quasi-linear evolution of the twice-shocked interface and the nonlinear evolution of the twice-shocked interface.

3.2.1. *Evolution law of once-shocked interface*

Understanding the evolution law of the once-shocked interface is essential for investigating S-RMI since the pre-reshock interface serves as the 'initial interface' for reshock. For the linear amplitude growth rate of the once-shocked interface ($\dot{a}^l_1$), the impulsive model proposed by Richtmyer (1960) is used to provide a theoretical reference ($\dot{a}^l_{1,i}$, with subscript 'i' denoting parameters predicted by the impulsive model) for the experimental result ($\dot{a}^l_{1,e}$). For the once-shocked interface, the impulsive model can be written as

$$\dot{a}^l_{1,i} = C_1 k a_0 A_1 u_{1,o}, \tag{3.1}$$

where $C_1 = 1 - u_{1,o}/v^i_{1,e}$ is the first shock compression factor, with v^i_1 being the velocity of IS_1. Here $\dot{a}^l_{1,e}$ is determined by linearly fitting the early-time variation of the once-shocked interface amplitude (a_1) measured from experiments. As shown in table 2, $\dot{a}^l_{1,e}$ agrees well with $\dot{a}^l_{1,i}$.

Referring to previous studies (Liu *et al.* 2018; Chen *et al.* 2023), the theoretical model constructed by Zhang & Guo (2016) (ZG model) is employed to provide a theoretical reference for the nonlinear evolution law of the once-shocked interface, which can be written as

$$\dot{a}^{b/s}_{1,zg}(t) = \frac{\dot{a}^l_{1,i}}{1 + \theta^{b/s}_1 k \dot{a}^l_{1,i} t}. \tag{3.2}$$

Here,

$$\theta^{b/s}_1 = \frac{3}{4}\frac{(1 \pm A_1)(3 \pm A_1)}{3 \pm A_1 + \sqrt{2}(1 \pm A_1)^{1/2}}\frac{4(3 \pm A_1) + \sqrt{2}(9 \pm A_1)(1 \pm A_1)^{1/2}}{(3 \pm A_1)^2 + 2\sqrt{2}(3 \mp A_1)(1 \pm A_1)^{1/2}}, \tag{3.3}$$

with superscripts 'b' and 's' denoting parameters of the bubble and spike, respectively, and subscript 'zg' representing parameters predicted by the ZG model. The ZG model

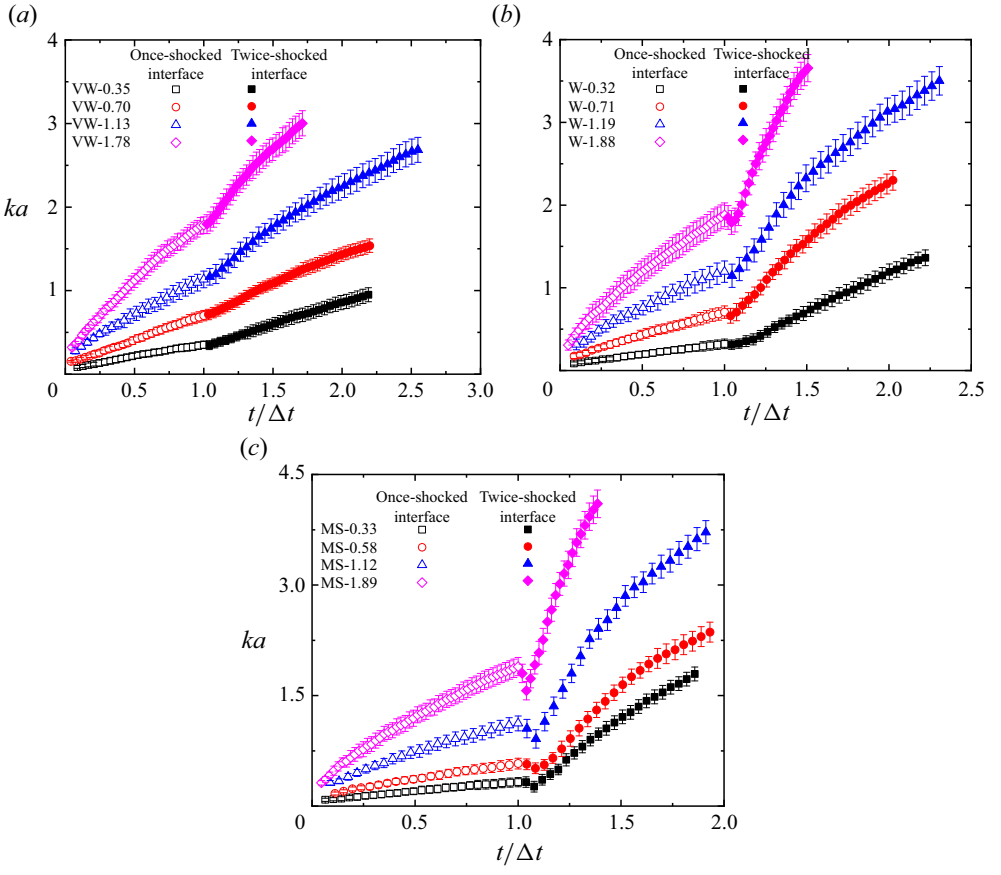

Figure 5. Temporal variations of scaled perturbation amplitude obtained from experiments: (*a*) cases VW; (*b*) cases W; (*c*) cases MS.

Case	$ka^r_{1,zg}$	$\dot{a}^l_{1,e}$	$\dot{a}^l_{1,i}$	$\dot{a}^r_{1,e}$	$\dot{a}^r_{1,zg}$	$k_I a_I/ka^r_{1,e}$	$k_{II}a_{II}/ka^r_{1,e}$
VW-0.35	0.36	3.07 ± 0.10	3.11	2.48	2.58	0.96	0.12
VW-0.70	0.71	5.42 ± 0.32	5.64	4.08	4.01	0.92	0.25
VW-1.13	1.15	8.51 ± 0.48	8.83	5.02	5.19	0.97	0.54
VW-1.78	1.72	9.16 ± 0.57	9.10	4.23	4.12	—	—
W-0.32	0.31	3.22 ± 0.43	2.90	2.46	2.39	0.96	0.13
W-0.71	0.72	6.16 ± 0.48	6.20	4.36	4.37	0.96	0.24
W-1.19	1.24	9.76 ± 0.50	9.90	5.42	5.68	0.98	0.52
W-1.88	1.83	8.71 ± 0.36	8.72	3.78	3.74	—	—
MS-0.33	0.34	2.78 ± 0.24	2.85	2.30	2.39	0.96	0.07
MS-0.58	0.60	5.56 ± 0.63	5.54	4.15	4.18	0.97	0.20
MS-1.12	1.19	8.37 ± 0.69	8.89	5.02	5.25	0.97	0.46
MS-1.89	1.90	8.74 ± 0.27	8.94	3.72	3.70	—	—

Table 2. Experimental and theoretical results for the evolution of the once-shocked interface: $a^r_{1,zg}$, pre-reshock amplitude predicted by the ZG model; $\dot{a}^l_{1,e}$ and $\dot{a}^l_{1,i}$, linear amplitude growth rates of the once-shocked interface obtained from experiments and predicted by impulsive model, respectively; $\dot{a}^r_{1,e}$ and $\dot{a}^r_{1,zg}$, pre-reshock amplitude growth rates obtained from experiments and predicted by ZG model, respectively; $k_I a_I$ and $k_{II}a_{II}$, scaled amplitudes of the fundamental and second-order modes, respectively.

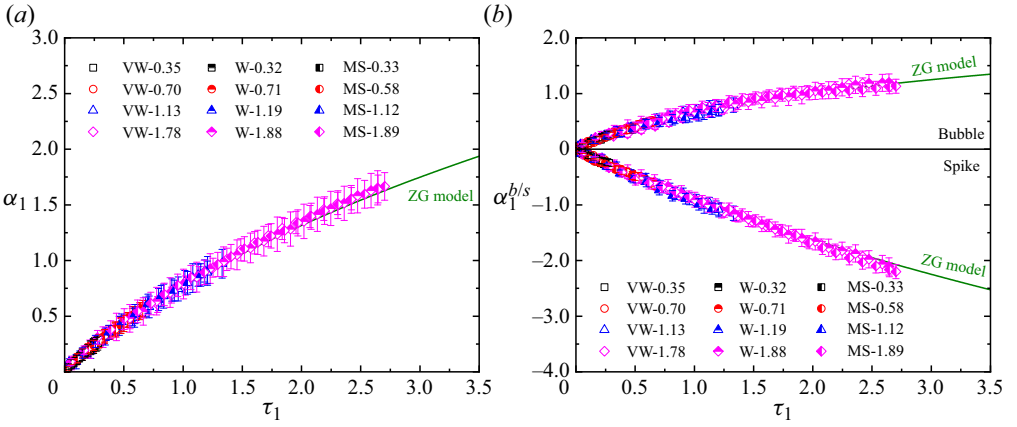

Figure 6. Experimental and theoretical results of the amplitude evolutions of the once-shocked interface (*a*) and its bubble and spike (*b*).

is applied once the start-up process (Yang, Zhang & Sharp 1994; Lombardini & Pullin 2009) concludes, and the duration of this process (t_1^*) as well as a_1 at $t = t_1^*$ (a_1^*) are calculated using methods proposed by Lombardini & Pullin (2009). Figure 6(*a*) shows the temporal variations of a_1, obtained from experiments and predicted by the ZG model, in dimensionless form. Here, t and a_1 are normalized as $\tau_1 = k\dot{a}_{1,i}^l(t - t_1^*)$ and $\alpha_1 = k(a_1 - a_1^*)$, respectively. Moreover, the temporal variations of the bubble and spike amplitudes of the once-shocked interface in dimensionless form (α_1^b and α_1^s) are shown in figure 6(*b*). The scaling collapses the results of all experiments, indicating that the once-shocked interface exhibits similar evolution laws across different cases. Besides, the ZG model provides excellent predictions for the evolutions of the overall, bubble and spike amplitudes of the once-shocked interface across all cases.

Next, the characteristics of the pre-reshock interface are explored. Determining the pre-reshock interface profile is highly challenging in experiments using the explosion-driven scheme to generate successive shocks (Buttler *et al.* 2014*a*,*b*). In contrast, in the present work, the pre-reshock interface profile can be clearly captured. Fast Fourier transform is applied to obtain the modal information (amplitude, phase and frequency) of the pre-reshock interface. Since fast Fourier transform is inapplicable when the interface cannot be expressed by a single-valued function, only the results of the cases with reshock occurring at the linear, weakly nonlinear and moderately nonlinear stages are provided. In addition, since the magnitudes of the third-order and other higher-order modes are negligible relative to that of the fundamental mode before the roll-up structures emerge (Liu *et al.* 2018), only the results of the fundamental and second-order modes are presented. The wavenumbers (amplitudes) of the fundamental and second-order modes are represented as k_I and k_{II} (a_I and a_{II}), respectively. Note that k_I and k_{II} are equivalent to k and $2k$, respectively. Table 2 shows the ratios of the scaled amplitudes of the fundamental and second-order modes to that of the overall pre-reshock interface ($k_I a_I/ka_{1,e}^r$ and $k_{II}a_{II}/ka_{1,e}^r$). For cases with reshock occurring at the linear evolution stage of the once-shocked interface, $k_{II}a_{II}/ka_{1,e}^r$ is notably lower than $k_I a_I/ka_{1,e}^r$ and $ka_{1,e}^r$ still satisfies the small-amplitude criterion (i.e. $ka \ll 1$). In contrast, in cases where reshock occurs at the nonlinear evolution stage of the once-shocked interface, $k_{II}a_{II}/ka_{1,e}^r$ is generally higher than 0.2 and $ka_{1,e}^r$ deviates from the small-amplitude criterion. Overall, the evolution state of the pre-reshock interface reflects the extent to which it deviates

from a small-amplitude single-mode one. In previous research on reflected-reshock RMI (Balasubramanian *et al.* 2012; Reilly *et al.* 2015; Guo *et al.* 2022*a*,*b*), it was found that the morphology and amplitude of the pre-reshock interface affect the post-reshock flow evolution. Therefore, it can be preliminarily inferred that in S-RMI, the shape effect of the pre-reshock interface would also influence the post-reshock perturbation development, warranting further detailed investigation.

Finally, the amplitude growth rate of the once-shocked interface at the onset of reshock, i.e. the pre-reshock amplitude growth rate ($\dot{a}_1^r$), which contributes to $\dot{a}_2^l$, is investigated. The experimental $\dot{a}_1^r$ ($\dot{a}_{1,e}^r$) is obtained by fitting the pre-reshock amplitude evolution of the once-shocked interface, and its theoretical reference ($\dot{a}_{1,zg}^r$) is calculated using the ZG model. Table 2 shows that $\dot{a}_{1,zg}^r$ closely matches $\dot{a}_{1,e}^r$, further indicating the effectiveness of using the ZG model to predict the evolution of the once-shocked interface. Additionally, $\dot{a}_{1,zg}^r$ is compared with $\dot{a}_{1,i}^l$. In cases where reshock occurs at the linear evolution stage of the once-shocked interface, the difference between $\dot{a}_{1,zg}^r$ and $\dot{a}_{1,i}^l$ is limited. However, in cases with reshock occurring at the nonlinear evolution stage of the once-shocked interface, the discrepancy between $\dot{a}_{1,zg}^r$ and $\dot{a}_{1,i}^l$ is significant, suggesting that the nonlinearity of the pre-reshock amplitude growth may also affect the post-reshock interface evolution. Overall, for S-RMI with reshock occurring at the nonlinear evolution stage of the once-shocked interface, further investigation is needed to ascertain whether and how the shape of the pre-reshock interface and its nonlinear amplitude growth affect the perturbation evolution of the twice-shocked interface.

3.2.2. *Quasi-linear amplitude growth of twice-shocked interface*

To predict $\dot{a}_2^l$, Mikaelian (1985) first proposed the linear superposition model which assumes that both $\dot{a}_1^l$ and $\Delta\dot{a}$ can be predicted by the impulsive model and that $\dot{a}_2^l$ is equal to their linear superposition. The model can be written as

$$\dot{a}_{2,ls}^l = \dot{a}_{1,i}^l + \Delta\dot{a}_i = \dot{a}_{1,i}^l + C_2 k a_{1,zg}^r A_2 (u_{2,o} - u_{1,o}), \tag{3.4}$$

where $\Delta\dot{a}_i$ denotes $\Delta\dot{a}$ predicted by the impulsive model; $u_{2,o}$ is the velocity of the twice-shocked interface predicted by one-dimensional gas dynamics theory; $C_2 = 1 - (u_{2,o} - u_{1,o})/(v_{2,e}^i - u_{1,o})$ is the reshock compression factor, with $v_{2,e}^i$ being the velocity of IS_2 obtained from experiment; and $a_{1,zg}^r$ represents a_1^r predicted by the ZG model and can be written as

$$a_{1,zg}^r = a_1^* + \int_{t_1^*}^{\Delta t} \frac{\dot{a}_{1,zg}^b(t) + \dot{a}_{1,zg}^s(t)}{2} \mathrm{d}t. \tag{3.5}$$

As shown in tables 1 and 2, $u_{2,o}$ and $ka_{1,zg}^r$ agree well with their experimental counterparts. Notably, since the linear superposition model assumes that $\Delta\dot{a}$ can be predicted by the impulsive model, it is theoretically valid only when the pre-reshock interface still satisfies the small-amplitude criterion. Building upon the linear superposition model, Wang *et al.* (2022) proposed a modified model that additionally considers the high-amplitude effect of the pre-reshock interface (H model). The H model can be expressed as

$$\dot{a}_{2,h}^l = \dot{a}_{1,i}^l + R_{dr}\Delta\dot{a}_i = \dot{a}_{1,i}^l + R_{dr} C_2 k a_{1,zg}^r A_2 (u_{2,o} - u_{1,o}), \tag{3.6}$$

where $R_{dr} = 1/[1 + (ka_{1,zg}^r/3)^{4/3}]$ is the theoretical reduction factor proposed by Dimonte & Ramaprabhu (2010) for describing the high-amplitude effect in single-shock RMI

Case	$\dot{a}^l_{2,e}$	$\dot{a}^l_{2,ls}$	$\dot{a}^l_{2,h}$	$\dot{a}^l_{2,nh}$	$a^{r,b}_{1,zg}$	$a^{r,s}_{1,zg}$	$\dot{a}^{r,b}_{1,zg}$	$\dot{a}^{r,s}_{1,zg}$	$\dot{a}^{l,b}_{2,e}$	$\dot{a}^{l,s}_{2,e}$	$\dot{a}^{l,b}_{2,em}$	$\dot{a}^{l,s}_{2,em}$	$\dot{a}^{l}_{2,em}$
VW-0.35	5.20 ± 0.19	6.01	5.85	5.32	1.64	1.81	2.26	2.90	4.45 ± 0.30	5.96 ± 0.80	4.64	5.80	5.22
VW-0.70	6.70 ± 0.47	9.23	8.77	7.15	3.08	3.68	3.13	4.89	4.76 ± 0.78	8.68 ± 0.36	5.16	8.03	6.60
VW-1.13	10.73 ± 0.62	19.02	16.79	13.15	3.20	4.15	3.61	6.77	7.25 ± 0.26	13.41 ± 0.70	7.37	14.12	10.75
VW-1.78	9.01 ± 0.51	23.75	19.01	14.03	4.34	6.64	2.38	5.85	5.51 ± 0.44	12.72 ± 0.82	5.65	12.97	9.31
W-0.32	12.38 ± 0.59	13.08	12.60	12.10	1.43	1.54	2.15	2.64	11.14 ± 1.52	12.94 ± 0.54	10.64	12.81	11.72
W-0.71	21.42 ± 0.66	30.41	27.27	25.44	3.12	3.74	3.41	5.33	16.55 ± 0.78	26.58 ± 0.36	15.86	26.10	20.98
W-1.19	23.12 ± 1.03	49.85	40.48	36.26	3.37	4.50	3.81	7.55	15.64 ± 1.80	30.64 ± 1.50	15.30	31.91	23.60
W-1.88	19.88 ± 1.01	66.69	46.94	41.96	4.52	7.12	2.11	5.38	12.82 ± 1.19	25.80 ± 1.66	11.93	27.39	19.66
MS-0.33	23.63 ± 1.34	28.17	26.83	26.37	1.57	1.72	2.11	2.67	19.59 ± 1.39	27.08 ± 1.19	20.37	26.86	23.62
MS-0.58	32.27 ± 1.30	48.20	43.70	42.34	2.69	3.08	3.42	4.94	25.70 ± 1.39	39.71 ± 0.61	24.10	40.05	32.07
MS-1.12	35.71 ± 0.93	96.74	76.94	73.31	3.27	4.30	3.57	6.93	22.54 ± 1.20	48.25 ± 1.78	21.39	48.33	34.86
MS-1.89	30.51 ± 1.90	147.03	98.45	93.21	4.66	7.42	2.07	5.34	18.29 ± 0.93	42.10 ± 1.19	16.45	38.86	27.65

Table 3. Experimental and theoretical results related to the pre-reshock amplitude evolution and post-reshock linear amplitude growth: $\dot{a}^l_{2,e}$, $\dot{a}^l_{2,ls}$, $\dot{a}^l_{2,h}$ and $\dot{a}^l_{2,nh}$, $\dot{a}^l_2$ obtained from experiments and predicted by linear superposition, H and NH models, respectively; $a^{r,b}_{1,zg}$ and $a^{r,s}_{1,zg}$ ($\dot{a}^{r,b}_{1,zg}$ and $\dot{a}^{r,s}_{1,zg}$), amplitudes (amplitude growth rates) of the pre-reshock bubble and spike predicted by the ZG model, respectively; $\dot{a}^{l,b}_{2,e}$ and $\dot{a}^{l,s}_{2,e}$, post-reshock linear amplitude growth rates of the bubble and spike extracted from experiments, respectively; $\dot{a}^{l,b}_{2,em}$, $\dot{a}^{l,s}_{2,em}$ and $\dot{a}^{l}_{2,em}$, post-reshock linear amplitude growth rates of the bubble, spike and overall interface predicted by the EM model, respectively.

at a single-mode interface. Note that other theoretical reduction factors proposed for single-shock RMI (Rikanati *et al.* 2003; Buttler *et al.* 2012; Probyn *et al.* 2021) are not considered in this study as their values closely approximate that of R_{dr} (Wang *et al.* 2023*b*). The H model has been demonstrated to outperform the linear superposition model for predicting $\dot{a}^l_2$ in S-RMI with a weak second shock and $ka^r_{1,e} < 2/3$ (Wang *et al.* 2022). Based on the H model, we propose a further modified model that accounts for the nonlinearity of the pre-reshock amplitude growth (NH model), which can be written as

$$\dot{a}^l_{2,nh} = \dot{a}^r_{1,zg} + R_{dr}\Delta\dot{a}_i = \dot{a}^r_{1,zg} + R_{dr}C_2 k a^r_{1,zg} A_2(u_{2,o} - u_{1,o}). \tag{3.7}$$

The $\dot{a}^l_2$ obtained from experiments ($\dot{a}^l_{2,e}$) and predicted by the linear superposition, H and NH models ($\dot{a}^l_{2,ls}$, $\dot{a}^l_{2,h}$ and $\dot{a}^l_{2,nh}$) are provided in table 3 for comparison. These models exhibit poorer performance when the nonlinearity of the pre-reshock interface evolution is more significant and/or the second shock is stronger. Moreover, none of these models are universally applicable under the considered reshock conditions. Nevertheless, the NH model generally offers the most accurate prediction for $\dot{a}^l_{2,e}$, highlighting the need to account for both the shape effect of the pre-reshock interface and the nonlinearity of its evolution. For cases VW, the secondary compression effect is weak, and the deviation of $\dot{a}^l_{2,e}$ from $\dot{a}^l_{2,nh}$ can directly reflect the applicability of R_{dr} in describing the shape effect of the pre-reshock interface. In cases VW-0.35 and VW-0.70, the NH model accurately predicts $\dot{a}^l_{2,e}$, suggesting that R_{dr} can well describe the pre-reshock interface shape effect when reshock occurs at the linear or weakly nonlinear evolution stage of the once-shocked interface. However, in cases VW-1.13 and VW-1.78, the NH model overestimates $\dot{a}^l_{2,e}$, indicating that R_{dr} is inadequate to describe the shape effect of the pre-reshock interface when it deviates significantly from a small-amplitude single-mode one. This overestimation may be attributed to the non-single-mode profile of the pre-reshock interface (Liang *et al.* 2019; Luo *et al.* 2020). For cases W, the NH

model predicts $\dot{a}^l_{2,e}$ well (poorly) when reshock occurs at the linear (nonlinear) evolution stage of the once-shocked interface. It is worth noting that R_{dr} is close in magnitude to the reduction factor derived for RMI in incompressible flow (Velikovich & Dimonte 1996). Therefore, the failure of R_{dr} to describe the reduction of the experimental $\Delta\dot{a}$ ($\Delta\dot{a}_e$) relative to $\Delta\dot{a}_i$ in case W-0.71 should be attributed to the secondary compression effect, which is negligible in case W-0.32 (VW-0.70) due to the low $ka^r_{1,e}$ (M_2). For cases W-1.19 and W-1.88, the combined influence of the pre-reshock interface shape effect and the secondary compression effect on $\Delta\dot{a}_e$ results in $\dot{a}^l_{2,e}$ being significantly lower than $\dot{a}^l_{2,nh}$. In cases MS, the coupling of these two effects has a more significant influence on $\Delta\dot{a}_e$ compared with that in cases W, and the secondary compression effect is non-negligible even when reshock occurs at the linear evolution stage of the once-shocked interface. Overall, both the pre-reshock interface shape effect and the secondary compression effect suppress the post-reshock linear amplitude growth and they would couple with each other. Furthermore, R_{dr} fails to accurately describe the reduction in $\Delta\dot{a}_e$ relative to $\Delta\dot{a}_i$ when either effect is significant.

Developing a theoretical model capable of accurately predicting $\dot{a}^l_{2,e}$ under various reshock conditions is desirable. However, providing a rigorous description of the coupling of the pre-reshock interface shape effect and secondary compression effect is challenging. Therefore, we seek to propose an empirical model based on the present experimental results. Due to nonlinearity, the bubble and spike generally have different amplitudes and amplitude growth rates before reshock. Consequently, their post-reshock linear amplitude growth rates ($\dot{a}^{l,b}_2$ and $\dot{a}^{l,s}_2$) should also differ and require separate consideration. Building on the NH model, an empirical model considering the coupling of the pre-reshock interface shape effect and the secondary compression effect (EM model) is proposed, which can be written as

$$\begin{aligned}\dot{a}^l_{2,em} &= \frac{\dot{a}^{l,b}_{2,em} + \dot{a}^{l,s}_{2,em}}{2} \\ &= \frac{[\dot{a}^{r,b}_{1,zg} + R^b_{em}C_2ka^{r,b}_{1,zg}A_2(u_{2,o}-u_{1,o})] + [\dot{a}^{r,s}_{1,zg} + R^s_{em}C_2ka^{r,s}_{1,zg}A_2(u_{2,o}-u_{1,o})]}{2},\end{aligned} \tag{3.8}$$

where

$$R^b_{em} = \frac{1}{1+\left\{ka^{r,b}_{1,zg}\dfrac{\sqrt{5[1+(u_{2,o}-u_{1,o})/(v^t_{2,o}-u_{2,o})]}}{2}\right\}^2}; \tag{3.9}$$

$$R^s_{em} = \frac{1}{1+\left\{ka^{r,s}_{1,zg}\dfrac{\sqrt{5[1+(u_{2,o}-u_{1,o})/(v^t_{2,o}-u_{2,o})]}}{4}\right\}^2}. \tag{3.10}$$

Here, $\dot{a}^{l,b}_{2,em}$ and $\dot{a}^{l,s}_{2,em}$ correspond to $\dot{a}^{l,b}_2$ and $\dot{a}^{l,s}_2$ predicted by the EM model, respectively; $a^{r,b}_{1,zg}$ and $a^{r,s}_{1,zg}$ ($\dot{a}^{r,b}_{1,zg}$ and $\dot{a}^{r,s}_{1,zg}$) represent the amplitudes (amplitude growth rates) of the pre-reshock bubble and spike predicted by the ZG model, respectively; R^b_{em} and R^s_{em} are the empirical factors utilized to describe the reduction in the reshock-induced

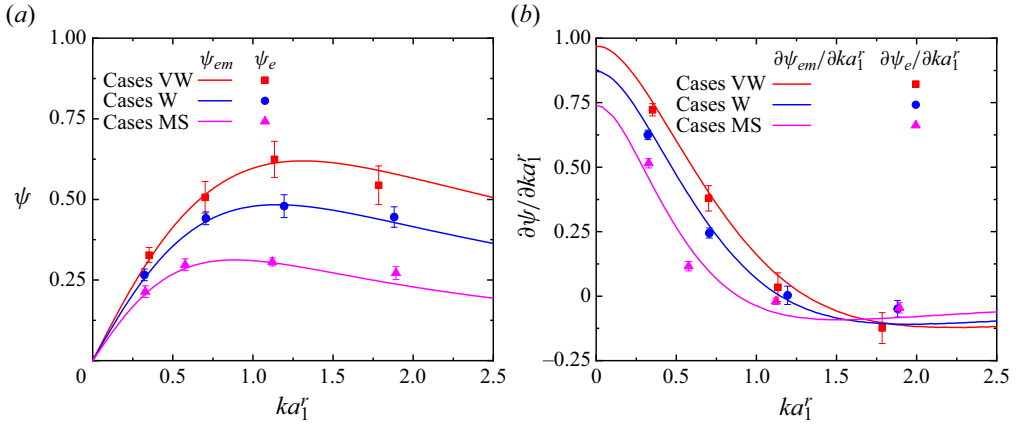

Figure 7. Variations of ψ (*a*) and $\partial\psi/\partial ka_1^r$ (*b*) with ka_1^r.

linear amplitude growth rates of the bubble and spike, respectively; and $v_{2,o}^t$ denotes the velocity of TS_2 predicted by the one-dimensional gas dynamics theory. In R_{em}^b (R_{em}^s), $ka_{1,zg}^{r,b}$ ($ka_{1,zg}^{r,s}$) is employed to depict the shape effect of the pre-reshock bubble (spike), while $(u_{2,o} - u_{1,o})/(v_{2,o}^t - u_{2,o})$ is introduced to describe the secondary compression effect. Notably, the form of the latter is referenced to a parameter used to characterize the dependence of linear amplitude evolution on shock intensity in single-shock RMI studies (Holmes *et al.* 1999; Glendinning *et al.* 2003). Experimental $\dot{a}_2^{l,b}$ and $\dot{a}_2^{l,s}$ ($\dot{a}_{2,e}^{l,b}$ and $\dot{a}_{2,e}^{l,s}$) are determined via using the position of the unperturbed interface, calculated by the one-dimensional gas dynamics theory, to distinguish the bubble and spike. As shown in table 3, $\dot{a}_{2,em}^{l,b}$, $\dot{a}_{2,em}^{l,s}$ and $\dot{a}_{2,em}^{l}$ align well with $\dot{a}_{2,e}^{l,b}$, $\dot{a}_{2,e}^{l,s}$ and $\dot{a}_{2,e}^{l}$, respectively, demonstrating the validity of the EM model under various reshock conditions considered in this study.

The dependence of $\Delta\dot{a}$ on ka_1^r is further analysed by introducing a correlation coefficient defined as

$$\psi = \frac{\Delta\dot{a}}{A_2(u_{2,o} - u_{1,o})}. \tag{3.11}$$

The variation rate of ψ with ka_1^r, i.e. $\partial\psi/\partial ka_1^r$, clearly illustrates the correlation between $\Delta\dot{a}$ and ka_1^r. If $|\partial\psi/\partial ka_1^r|$ is close to 0 (1), it indicates a weak (strong) correlation between $\Delta\dot{a}$ and ka_1^r. Additionally, a positive (negative) $\partial\psi/\partial ka_1^r$ suggests a positive (negative) correlation between $\Delta\dot{a}$ and ka_1^r. The results for ψ and $\partial\psi/\partial ka_1^r$ obtained from experiments (ψ_e and $\partial\psi_e/\partial ka_1^r$), along with the corresponding predictions from the EM model (ψ_{em} and $\partial\psi_{em}/\partial ka_1^r$), are shown in figure 7. It can be observed that the correlation between $\Delta\dot{a}$ and ka_1^r changes from strongly positive to weakly positive and then to weakly negative as ka_1^r increases, regardless of the intensity of the second shock. This indicates that $\Delta\dot{a}$ is non-monotonically related to ka_1^r, and that this relationship is primarily due to the shape effect of the pre-reshock interface. Additionally, the correlation between $\Delta\dot{a}$ and ka_1^r is weaker when the second shock is stronger, due to the suppression of the secondary compression effect on post-reshock amplitude evolution.

3.2.3. *Nonlinear amplitude growth of twice-shocked interface*

Following a short period of linear growth, the amplitude of the twice-shocked interface enters the nonlinear evolution stage. Currently, a rigorous theory for describing the post-reshock nonlinear amplitude evolution is still lacking. In previous studies on S-RMI (Karkhanis *et al.* 2017; Karkhanis & Ramaprabhu 2019; Wang *et al.* 2022), some nonlinear models proposed for single-shock RMI have been utilized to predict the nonlinear perturbation growth of the twice-shocked interface. Wang *et al.* (2022) found that the ZG model is applicable to predict the post-reshock amplitude evolution when the second shock is weak and reshock occurs at the linear evolution stage of the once-shocked interface. In this work, the ZG model is similarly adopted to offer a theoretical reference for the nonlinear perturbation growth of the twice-shocked interface, which can be rewritten as

$$\dot{a}_{2,zg}^{b/s}(t) = \frac{\dot{a}_{2,em}^{l,b/s}}{1 + \theta_2^{b/s} k \dot{a}_{2,em}^{l,b/s} t}, \tag{3.12}$$

where

$$\theta_2^{b/s} = \frac{3}{4} \frac{(1 \pm A_2)(3 \pm A_2)}{3 \pm A_2 + \sqrt{2}(1 \pm A_2)^{1/2}} \frac{4(3 \pm A_2) + \sqrt{2}(9 \pm A_2)(1 \pm A_2)^{1/2}}{(3 \pm A_2)^2 + 2\sqrt{2}(3 \mp A_2)(1 \pm A_2)^{1/2}}. \tag{3.13}$$

Figure 8 illustrates the temporal variations of the bubble and spike amplitudes of the twice-shocked interface (a_2^b and a_2^s) in dimensionless form. The evolution time and amplitude of the bubble/spike are normalized as $\tau_2^{b/s} = k\dot{a}_{2,em}^{l,b/s}(t - t_2^{b*/s*})$ and $\alpha_2^{b/s} = k(a_2^{b/s} - a_2^{b*/s*})$, respectively, in which $t_2^{b*/s*}$ indicates the moment when the linear growth of $a_2^{b/s}$ starts in the experiment, and $a_2^{b*/s*}$ is the corresponding $a_2^{b/s}$ at $t = t_2^{b*/s*}$. As the ZG model does not account for the initial amplitude effect, its predictions for cases with similar second shock intensities but different $ka_{1,e}^r$ are highly consistent. Accordingly, only two theoretical lines, corresponding to the bubble and spike of the twice-shocked interface, respectively, are provided in each figure. The scaling effectively collapses the results of cases with similar second shock intensities. For cases VW and W, the ZG model accurately predicts the overall bubble and spike evolutions. However, for cases MS, the ZG model overestimates the bubble growth while underestimating the spike development from the intermediate to late stages. These results suggest that the ZG model can reasonably describe the post-reshock nonlinear amplitude evolution when the second shock is very weak/weak, and the secondary compression effect could alter the nonlinear evolution law of the twice-shocked interface when the second shock reaches a certain intensity. Specifically, the high pressure generated by interactions among transverse shock waves inhibits (promotes) the bubble (spike) growth, leading to the overestimation (underestimation) of the ZG model.

Further, we attempt to propose an empirical nonlinear model based on the ZG model and present experimental results, aiming to effectively describe the post-reshock nonlinear evolution law under all reshock conditions considered. For the evolutions of the bubble and spike of the twice-shocked interface, the empirical model (mZG model), obtained after many attempts, can be respectively written as

$$\dot{a}_{2,mzg}^{b}(t) = \frac{\dot{a}_{2,em}^{l,b}}{1 + \theta_2^{b} k \dot{a}_{2,em}^{l,b} F^b t} \tag{3.14}$$

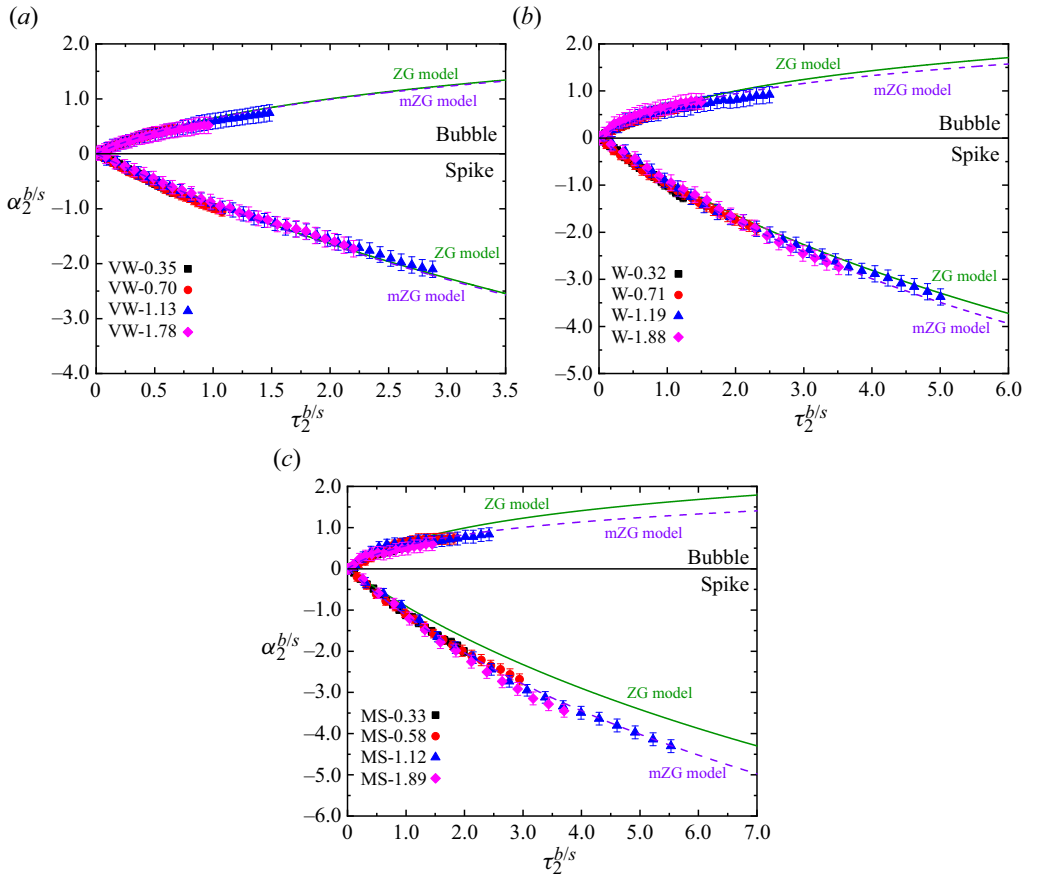

Figure 8. Experimental and theoretical results on the amplitude evolutions of the bubble and spike of the twice-shocked interface: (*a*) cases VW, (*b*) cases W and (*c*) cases MS.

and

$$\dot{a}^{s}_{2,mzg}(t) = \frac{\dot{a}^{l,s}_{2,em}F^{s}}{1+\theta^{s}_{2}k\dot{a}^{l,s}_{2,em}F^{s}t}. \tag{3.15}$$

Here, $F^{b} = 1 + (u_{2,o} - u_{1,o})/3(v^{t}_{2,o} - u_{2,o})$ and $F^{s} = 1 + (u_{2,o} - u_{1,o})/5(v^{t}_{2,o} - u_{2,o})$ represent the empirical factors for describing the secondary compression effect on the post-reshock growths of the bubble and spike, respectively. As illustrated in figure 8, the mZG model accurately predicts the overall bubble and spike evolutions for all cases, demonstrating its ability to precisely describe the nonlinear evolution law of the twice-shocked interface under the reshock conditions considered.

4. Conclusions and perspective

Richtmyer–Meshkov instability induced by two successive shock waves propagating in the same direction (S-RMI) under diverse reshock conditions is studied through shock-tube experiments. We aim to explore how the evolution law of the twice-shocked interface depends on the interface evolution state before reshock and second shock intensity.

Qualitatively, the reshock promotes the interface instability, and its effect is related to both the pre-reshock interface evolution state and second shock intensity. When the secondary compression effect introduced by transverse shock waves is significant, the heads of the bubbles gradually flatten out and eventually occupy nearly the entire space along the spanwise direction in the late stages.

Quantitatively, the linear and nonlinear amplitude evolutions of the once-shocked interface can be effectively predicted by the impulsive model (Richtmyer 1960) and the nonlinear model proposed by Zhang & Guo (2016) (ZG model), respectively. Besides, when reshock occurs at the moderately or strongly nonlinear evolution stage of the once-shocked interface, the pre-reshock interface no longer satisfies the small-amplitude criterion and deviates notably from a single-mode profile. For the linear evolution of the twice-shocked interface, models fail to provide accurate prediction when the pre-reshock interface has entered the moderately or strongly nonlinear evolution stage and/or the second shock reaches a certain intensity. This failure arises from the inadequacy of existing reduction factors in describing the pre-reshock interface shape effect and the secondary compression effect when either is significant. On the basis of the present experimental results and considering bubble and spike separately, an empirical linear model that accounts for the coupling of the pre-reshock interface shape effect and secondary compression effect is proposed. Furthermore, the reshock-induced amplitude growth rate exhibits a non-monotonic dependence on the scaled pre-reshock amplitude, primarily ascribed to the shape effect of the pre-reshock interface. This correlation weakens when the second shock is stronger due to the more pronounced secondary compression effect. For the nonlinear evolution of the twice-shocked interface, the ZG model offers reasonable predictions when the second shock is very weak/weak. However, when the second shock is moderately strong, the ZG model overestimates the bubble growth and underestimates the spike evolution under the influence of the significant secondary compression effect. Building on the current experimental findings and the ZG model, we propose an empirical nonlinear model that accurately describes the nonlinear evolution law of the twice-shocked interface under the reshock conditions considered.

This study investigates S-RMI with diverse pre-reshock interface evolution states and second shock intensities. However, the current experiments are conducted with roughly the same Atwood number and the intensity of the strongest second shock is only moderately strong. Extensive studies on single-shock RMI have shown that the instability evolution and predictive capabilities of models are related to both the sign and magnitude of the Atwood number (Jourdan & Houas 2005; Matsuoka & Nishihara 2006*a*,*b*; Mariani *et al.* 2008; Dimonte & Ramaprabhu 2010; Lombardini *et al.* 2011; Chen *et al.* 2023; Wang *et al.* 2023*a*,*b*). In addition, it has been observed that the evolution law of single-shock RMI remains sensitive to shock intensity in the regime where Mach number exceeds 1.5 (Holmes *et al.* 1999; Sadot *et al.* 2003; Puranik *et al.* 2004). Therefore, it can be inferred that variations in Atwood number and further enhancement of second shock intensity also affect the evolution law of the twice-shocked interface. Accordingly, the applicability of the empirical models proposed in this work to S-RMI with various Atwood numbers and stronger second shocks remains uncertain. To further evaluate and refine these models, experimental research on S-RMI across a broader range of reshock conditions will be conducted in the near future.

Furthermore, it is worth noting that both the large-scale perturbation evolution and small-scale material mixing contribute to the degradation of ICF implosion performance (Zhou 2017*a*,*b*, 2024). Thus, investigations on the large-scale perturbation evolution and small-scale mixing are both essential. In the present work, the schlieren technique is employed to capture the large-scale wave and interface evolution. However, this method

cannot provide additional quantitative flow information, such as the velocity and vorticity fields, and thus does not provide deeper insights regarding the small-scale mixing. Mixing diagnostics, such as PLIF, PIV and simultaneous PLIF/PIV techniques, have been utilized to study single-shock and reflected-reshock RMI at small scales (Balakumar *et al.* 2012; Balasubramanian *et al.* 2012; Mohaghar *et al.* 2017, 2019; Mansoor *et al.* 2020; Sewell *et al.* 2021). In future work, these more advanced diagnostics will be applied to reach an understanding of S-RMI from a more quantitative perspective, in the hope that our experiments can be more useful to the research community on shock waves and hydrodynamic instabilities.

Acknowledgements. The authors appreciate the valuable suggestions of the reviewers.

Funding. This work was supported by the National Natural Science Foundation of China (nos. 12102425, 12472228, 12372281, 91952205 and 12388101), Youth Innovation Promotion Association CAS, the Fundamental Research Funds for the Central Universities and Young Elite Scientists Sponsorship Program by CAST (no. 2023QNRC001).

Declaration of interests. The authors report no conflict of interest.

Author ORCIDs.
He Wang https://orcid.org/0000-0002-6497-6673;
Zhigang Zhai https://orcid.org/0000-0002-0094-5210;
Xisheng Luo https://orcid.org/0000-0002-4303-8290.

References

Abu-Shawareb, H., *et al.* 2022 Lawson criterion for ignition exceeded in an inertial fusion experiment. *Phys. Rev. Lett.* **129**, 075001.

Arnett, W.D., Bahcall, J.N., Kirshner, R.P. & Woosley, S.E. 1989 Supernova 1987A. *Annu. Rev. Astron. Astrophys.* **27**, 629–700.

Balakumar, B.J., Orlicz, G.C., Ristorcelli, J.R., Balasubramanian, S., Prestridge, K.P. & Tomkins, C.D. 2012 Turbulent mixing in a Richtmyer-Meshkov fluid layer after reshock: velocity and density statistics. *J. Fluid Mech.* **696**, 67–93.

Balakumar, B.J., Orlicz, G.C., Tomkins, C.D. & Prestridge, K.P. 2008 Simultaneous particle-image velocimetry-planar laser-induced fluorescence measurements of Richtmyer-Meshkov instability growth in a gas curtain with and without reshock. *Phys. Fluids* **20**, 124103.

Balasubramanian, S., Orlicz, G.C., Prestridge, K.P. & Balakumar, B.J. 2012 Experimental study of initial condition dependence on Richtmyer-Meshkov instability in the presence of reshock. *Phys. Fluids* **24**, 034103.

Betti, R. & Hurricane, O.A. 2016 Inertial-confinement fusion with lasers. *Nat. Phys.* **12**, 435–448.

Billig, F.S. 1993 Research on supersonic combustion. *J. Propul. Power* **9**, 499–514.

Buttler, W.T., *et al.* 2014*a* Explosively driven two-shockwave tools with applications. *J. Phys.: Conf. Ser.* **500**, 112014.

Buttler, W.T., *et al.* 2014*b* Second shock ejecta measurements with an explosively driven two-shockwave drive. *J. Appl. Phys.* **116**, 103519.

Buttler, W.T., *et al.* 2012 Unstable Richtmyer-Meshkov growth of solid and liquid metals in vacuum. *J. Fluid Mech.* **703**, 60–84.

Charakhch'yan, A.A. 2000 Richtmyer-Meshkov instability of an interface between two media due to passage of two successive shocks. *J. Appl. Mech. Tech. Phys.* **41**, 23–31.

Charakhch'yan, A.A. 2001 Reshocking at the non-linear stage of Richtmyer-Meshkov instability. *Plasma Phys. Control. Fusion* **43**, 1169–1179.

Chen, C., Xing, Y., Wang, H., Zhai, Z. & Luo, X. 2023 Experimental study on Richtmyer-Meshkov instability at a light-heavy interface over a wide range of Atwood numbers. *J. Fluid Mech.* **975**, A29.

Cherne, F.J., Hammerberg, J.E., Andrews, M.J., Karkhanis, V. & Ramaprabhu, P. 2015 On shock driven jetting of liquid from non-sinusoidal surfaces into a vacuum. *J. Appl. Phys.* **118**, 185901.

Collins, B.D. & Jacobs, J.W. 2002 PLIF flow visualization and measurements of the Richtmyer-Meshkov instability of an air/SF_6 interface. *J. Fluid Mech.* **464**, 113–136.

DIMONTE, G., FRERKING, C.E., SCHNEIDER, M. & REMINGTON, B. 1996 Richtmyer-Meshkov instability with strong radiatively driven shocks. *Phys. Plasmas* **3**, 614–630.

DIMONTE, G. & RAMAPRABHU, P. 2010 Simulations and model of the nonlinear Richtmyer-Meshkov instability. *Phys. Fluids* **22**, 014104.

GLASS, I.I. & HALL, J.G. 1959 Handbook of Supersonic Aerodynamics. Section 18. Shock tubes. *NAVORD* R-1488.

GLENDINNING, S.G., *et al.* 2003 Effect of shock proximity on Richtmyer-Meshkov growth. *Phys. Plasmas* **10**, 1931–1936.

GUO, X., CONG, Z., SI, T. & LUO, X. 2022*a* Shock-tube studies of single- and quasi-single-mode perturbation growth in Richtmyer-Meshkov flows with reshock. *J. Fluid Mech.* **941**, A65.

GUO, X., SI, T., ZHAI, Z. & LUO, X. 2022*b* Large-amplitude effects on interface perturbation growth in Richtmyer-Meshkov flows with reshock. *Phys. Fluids* **34**, 082118.

GUO, X., ZHAI, Z., DING, J., SI, T. & LUO, X. 2020 Effects of transverse shock waves on early evolution of multi-mode chevron interface. *Phys. Fluids* **32**, 106101.

HOLMES, R.L., DIMONTE, G., FRYXELL, B., GITTINGS, M.L., GROVE, J.W., SCHNEIDER, M., SHARP, D.H., VELIKOVICH, A.L., WEAVER, R.P. & ZHANG, Q. 1999 Richtmyer-Meshkov instability growth: experiment, simulation and theory. *J. Fluid Mech.* **389**, 55–79.

JOURDAN, G. & HOUAS, L. 2005 High-amplitude single-mode perturbation evolution at the Richtmyer-Meshkov instability. *Phys. Rev. Lett.* **95**, 204502.

KARKHANIS, V. & RAMAPRABHU, P. 2019 Ejecta velocities in twice-shocked liquid metals under extreme conditions: a hydrodynamic approach. *Matter Radiat. Extrem.* **4**, 044402.

KARKHANIS, V., RAMAPRABHU, P., BUTTLER, W.T., HAMMERBERG, J.E., CHERNE, F.J. & ANDREWS, M.J. 2017 Ejecta production from second shock: numerical simulations and experiments. *J. Dyn. Behav. Mater.* **3**, 265–279.

KARKHANIS, V., RAMAPRABHU, P., CHERNE, F.J., HAMMERBERG, J.E. & ANDREWS, M.J. 2018 A numerical study of bubble and spike velocities in shock-driven liquid metals. *J. Appl. Phys.* **123**, 025902.

KURANZ, C.C., *et al.* 2018 How high energy fluxes may affect Rayleigh–Taylor instability growth in young supernova remnants. *Nat. Commun.* **9**, 1564.

LEINOV, E., MALAMUD, G., ELBAZ, Y., LEVIN, L.A., BEN-DOR, G., SHVARTS, D. & SADOT, O. 2009 Experimental and numerical investigation of the Richtmyer-Meshkov instability under re-shock conditionse. *J. Fluid Mech.* **626**, 449–475.

LIANG, Y., ZHAI, Z., DING, J. & LUO, X. 2019 Richtmyer-Meshkov instability on a quasi-single-mode interface. *J. Fluid Mech.* **872**, 729–751.

LINDL, J., LANDEN, O., EDWARDS, J., MOSES, E. & TEAM, N. 2014 Review of the national ignition campaign 2009–2012. *Phys. Plasmas* **21**, 020501.

LIU, L., LIANG, Y., DING, J., LIU, N. & LUO, X. 2018 An elaborate experiment on the single-mode Richtmyer-Meshkov instability. *J. Fluid Mech.* **853**, R2.

LOMBARDINI, M., HILL, D.J., PULLIN, D.I. & MEIRON, D.I. 2011 Atwood ratio dependence of Richtmyer-Meshkov flows under reshock conditions using large-eddy simulations. *J. Fluid Mech.* **670**, 439–480.

LOMBARDINI, M. & PULLIN, D.I. 2009 Startup process in the Richtmyer-Meshkov instability. *Phys. Fluids* **21**, 044104.

LUO, X., LIU, L., LIANG, Y., DING, J. & WEN, C. 2020 Richtmyer-Meshkov instability on a dual-mode interface. *J. Fluid Mech.* **905**, A5.

MANSOOR, M.M., DALTON, S.M., MARTINEZ, A.A., DESJARDINS, T., CHARONKO, J.J. & PRESTRIDGE, K.P. 2020 The effect of initial conditions on mixing transition of the Richtmyer-Meshkov instability. *J. Fluid Mech.* **904**, A3.

MARIANI, C., VANDENBOOMGAERDE, M., JOURDAN, G., SOUFFLAND, D. & HOUAS, L. 2008 Investigation of the Richtmyer-Meshkov instability with stereolithographed interfaces. *Phys. Rev. Lett.* **100**, 254503.

MATSUOKA, C. & NISHIHARA, K. 2006*a* Analytical and numerical study on a vortex sheet in incompressible Richtmyer-Meshkov instability in cylindrical geometry. *Phys. Rev.* E **74**, 066303.

MATSUOKA, C. & NISHIHARA, K. 2006*b* Vortex core dynamics and singularity formations in incompressible Richtmyer-Meshkov instability. *Phys. Rev.* E **73**, 026304.

MCFARLAND, J.A., GREENOUGH, J.A. & RANJAN, D. 2013 Investigation of the initial perturbation amplitude for the inclined interface Richtmyer-Meshkov instability. *Phys. Scr.* **T155**, 014014.

MESHKOV, E.E. 1969 Instability of the interface of two gases accelerated by a shock wave. *Fluid Dyn.* **4**, 101–104.

MIKAELIAN, K.O. 1985 Richtmyer-Meshkov instabilities in stratified fluids. *Phys. Rev.* A **31**, 410–419.

MIKAELIAN, K.O. 1998 Analytic approach to nonlinear Rayleigh–Taylor and Richtmyer-Meshkov instabilities. *Phys. Rev. Lett.* **80**, 508–511.

MOHAGHAR, M., CARTER, J., MUSCI, B., REILLY, D., MCFARLAND, J. & RANJAN, D. 2017 Evaluation of turbulent mixing transition in a shock-driven variable-density flow. *J. Fluid Mech.* **831**, 779–825.

MOHAGHAR, M., CARTER, J., PATHIKONDA, G. & RANJAN, D. 2019 The transition to turbulence in shock-driven mixing: effects of Mach number and initial conditions. *J. Fluid Mech.* **871**, 595–635.

MOTL, B., OAKLEY, J., RANJAN, D., WEBER, C., ANDERSON, M. & BONAZZA, R. 2009 Experimental validation of a Richtmyer-Meshkov scaling law over large density ratio and shock strength ranges. *Phys. Fluids* **21**, 126102.

NUCKOLLS, J., WOOD, L., THIESSEN, A. & ZIMMERMAN, G. 1972 Laser compression of matter to super-high densities: thermonuclear (CTR) applications. *Nature* **239**, 139–142.

PANDIAN, A., STELLINGWERF, R.F. & ABARZHI, S.I. 2017 Effect of a relative phase of waves constituting the initial perturbation and the wave interference on the dynamics of strong-shock-driven Richtmyer-Meshkov flows. *Phys. Rev. Fluids* **2**, 073903.

PARK, H.-S., *et al.* 2014 High-adiabat high-foot inertial confinement fusion implosion experiments on the national ignition facility. *Phys. Rev. Lett.* **112**, 055001.

PROBYN, M.G., WILLIAMS, R.J.R., THORNBER, B., DRIKAKIS, D. & YOUNGS, D.L. 2021 2D single-mode Richtmyer-Meshkov instability. *Physica* D **418**, 132827.

PURANIK, P.B., OAKLEY, J.G., ANDERSON, M.H. & BONAZZA, R. 2004 Experimental study of the Richtmyer-Meshkov instability induced by a Mach 3 shock wave. *Shock Waves* **13**, 413–429.

REILLY, D., MCFARLAND, J., MOHAGHAR, M. & RANJAN, D. 2015 The effects of initial conditions and circulation deposition on the inclined-interface reshocked Richtmyer-Meshkov instability. *Exp. Fluids* **56**, 1–16.

RICHTMYER, R.D. 1960 Taylor instability in shock acceleration of compressible fluids. *Commun. Pure Appl. Maths* **13**, 297–319.

RIKANATI, A., ORON, D., SADOT, O. & SHVARTS, D. 2003 High initial amplitude and high Mach number effects on the evolution of the single-mode Richtmyer-Meshkov instability. *Phys. Rev.* E **67**, 026307.

SADOT, O., RIKANATI, A., ORON, D., BEN-DOR, G. & SHVARTS, D. 2003 An experimental study of the high Mach number and high initial-amplitude effects on the evolution of the single-mode Richtmyer-Meshkov instability. *Laser Part. Beams* **21**, 341–346.

SEWELL, E.G., FERGUSON, K.J., KRIVETS, V.V. & JACOBS, J.W. 2021 Time-resolved particle image velocimetry measurements of the turbulent Richtmyer-Meshkov instability. *J. Fluid Mech.* **917**, A41.

SMALYUK, V.A., *et al.* 2019 Review of hydrodynamic instability experiments in inertially confined fusion implosions on National Ignition Facility. *Plasma Phys. Control. Fusion* **62**, 014007.

STANIC, M., STELLINGWERF, R.F., CASSIBRY, J.T. & ABARZHI, S.I. 2012 Scale coupling in Richtmyer-Meshkov flows induced by strong shocks. *Phys. Plasmas* **19**, 082706.

UKAI, S., BALAKRISHNAN, K. & MENON, S. 2011 Growth rate predictions of single- and multi-mode Richtmyer-Meshkov instability with reshock. *Shock Waves* **21**, 533–546.

VELIKOVICH, A.L. & DIMONTE, G. 1996 Nonlinear perturbation theory of the incompressible Richtmyer-Meshkov instability. *Phys. Rev. Lett.* **76**, 3112–3115.

WANG, H., CAO, Q., CHEN, C., ZHAI, Z. & LUO, X. 2022 Experimental study on a light-heavy interface evolution induced by two successive shock waves. *J. Fluid Mech.* **953**, A15.

WANG, H., WANG, H., ZHAI, Z. & LUO, X. 2023*a* High-amplitude effect on Richtmyer-Meshkov instability at a single-mode heavy-light interface. *Phys. Fluids* **35**, 126107.

WANG, H., WANG, H., ZHAI, Z. & LUO, X. 2023*b* High-amplitude effect on single-mode Richtmyer-Meshkov instability of a light-heavy interface. *Phys. Fluids* **35**, 016106.

WILLIAMS, R.J.R. & GRAPES, C.C. 2017 Simulation of double-shock ejecta production. *J. Dyn. Behav. Mater.* **3**, 291–299.

WU, B., HE, A., WANG, X., SUN, H. & WANG, P. 2023 Numerical investigation of ejecta mass of twice-shocked liquid Sn. *J. Appl. Phys.* **133**, 165903.

YANG, J., KUBOTA, T. & ZUKOSKI, E.E. 1993 Applications of shock-induced mixing to supersonic combustion. *AIAA J.* **31**, 854–862.

YANG, Y., ZHANG, Q. & SHARP, D.H. 1994 Small amplitude theory of Richtmyer-Meshkov instability. *Phys. Fluids* **6**, 1856–1873.

ZHANG, J., *et al.* 2020 Double-cone ignition scheme for inertial confinement fusion. *Phil. Trans. R. Soc.* A **378**, 20200015.

ZHANG, Q. & GUO, W. 2016 Universality of finger growth in two-dimensional Rayleigh–Taylor and Richtmyer-Meshkov instabilities with all density ratios. *J. Fluid Mech.* **786**, 47–61.

ZHOU, Y. 2017*a* Rayleigh–Taylor and Richtmyer-Meshkov instability induced flow, turbulence, and mixing. I. *Phys. Rep.* **720-722**, 1–136.

ZHOU, Y. 2017*b* Rayleigh–Taylor and Richtmyer-Meshkov instability induced flow, turbulence, and mixing. II. *Phys. Rep.* **723–725**, 1–160.

ZHOU, Y. 2024 *Hydrodynamic Instabilities and Turbulence: Rayleigh–Taylor, Richtmyer-Meshkov, and Kelvin–Helmholtz Mixing*. Cambridge University Press.

ZHOU, Y., CLARK, T.T., CLARK, D.S., GLENDINNING, S.G., SKINNER, M.A., HUNTINGTON, C.M., HURRICANE, O.A., DIMITS, A.M. & REMINGTON, B.A. 2019 Turbulent mixing and transition criteria of flows induced by hydrodynamic instabilities. *Phys. Plasmas* **26**, 080901.

ZHOU, Y., *et al.* 2021 Rayleigh–Taylor and Richtmyer-Meshkov instabilities: a journey through scales. *Physica* D **423**, 132838.